

1 **High-resolution records of Oceanic Anoxic Event 2: Insights**
2 **into the timing, duration and extent of environmental**
3 **perturbations from the palaeo-South Pacific Ocean**
4

5 **Authors:** S.K. Gangl^{a,b,*}, C.M. Moy^c, C.H. Stirling^{a,b}, H.C. Jenkyns^d,
6 J.S. Crampton^{e,f}, M.O. Clarkson^{a,b,1}, C. Ohneiser^c, D. Porcelli^d

7 **Affiliations:**

8 ^a Department of Chemistry, University of Otago, PO Box 56, Dunedin, NZ

9 ^b Centre for Trace Element Analysis, University of Otago, PO Box 56, Dunedin, NZ

10 ^c Department of Geology, University of Otago, PO Box 56, Dunedin, NZ

11 ^d Department of Earth Sciences, University of Oxford, South Parks Road, Oxford OX1 3AN,
12 UK

13 ^e GNS Science, PO Box 30368, Lower Hutt, NZ

14 ^f School of Geography, Environment and Earth Sciences, Victoria University of Wellington,
15 PO Box 600, Wellington, NZ

16 ¹ Now at: Department of Earth Sciences, ETH Zürich, Clausiusstrasse 25, 9092 Zürich, CH

17 * Corresponding author: Sophie Gangl (sophie.gangl@otago.ac.nz)

18
19 Manuscript to be submitted to *Earth and Planetary Science Letters*

20 Main text word count: ca. 6,510 (excluding abstract, acknowledgements, references, table and
21 figure captions)

23 **Abstract**

24 Oceanic Anoxic Event 2 (OAE 2), which took place around the Cenomanian–Turonian
25 boundary (~94 Ma), is associated with extreme perturbations to the global carbon cycle,
26 affected ocean basins worldwide and was associated with significant biological turnover.
27 Although this event has been well studied in the northern hemisphere, the evolution and
28 character of OAE 2, particularly in terms of the vertical and lateral extent of anoxia, is poorly
29 constrained in the palaeo-Pacific Ocean. Furthermore, the precise timing, duration and
30 character of this event, and the exact mechanisms driving OAE 2 environmental changes, are
31 still being debated. Here, we present the first high-resolution records of carbon- isotopes, total
32 organic carbon and magnetic susceptibility from the southern palaeo-Pacific Ocean during
33 OAE 2, sampled at two sections in New Zealand. The carbon-isotope records from both
34 localities reveal a ~2 ‰ positive excursion that represents the global change in the carbon
35 cycle associated with OAE 2. When combined with a cyclostratigraphic age model, these new
36 records constrain the duration of the OAE 2 carbon-isotope excursion to at least 930 ± 25 ky
37 and indicate a minimum duration of 200 ± 25 ky for the ‘Plenus Cold Event’ that took place
38 during OAE 2. The lithologies and low organic-carbon contents of the New Zealand sections
39 imply that oxic conditions prevailed along, at least parts of, the margins of the palaeo-Pacific
40 Ocean at mid- to high southern latitudes during OAE 2 while, contemporaneously, conditions
41 were locally anoxic in the mid-water column of the equatorial Pacific Ocean. Despite these
42 apparently oxic conditions in the New Zealand region, there was a partial collapse of benthic
43 ecosystems leading up to, and during, OAE 2, suggesting environmental deterioration caused
44 by intermittent oxygen deprivation, or other chemical or biological disturbances in the South
45 Pacific region that remain to be elucidated.

46

47 **KEYWORDS:**

48 Oceanic Anoxic Event 2, Carbon-isotope excursion, Cretaceous, Organic carbon, Orbital
49 forcing, Cenomanian–Turonian

50

51 **MAIN TEXT:**

52

53 **1. Introduction**

54 The Oceanic Anoxic Events (OAEs) of the Mesozoic Era are well-known
55 palaeoenvironmental phenomena that represent major disturbances of the global carbon cycle
56 and were characterised by the burial of vast amounts of marine organic matter in all ocean
57 basins, often preserved as ‘black shales’ (Schlanger and Jenkyns, 1976). OAEs were closely
58 linked to the rapid influx of CO₂ into the atmosphere, which in turn drove abrupt global
59 warming and increased weathering, thereby increasing the supply of nutrients to the oceans
60 (e.g. Turgeon and Creaser, 2008; Du Vivier et al., 2014; Jenkyns et al., 2017; Clarkson et al.,
61 2018). This process in turn stimulated plankton productivity and accentuated the flux of
62 organic matter through the water column. The decomposition of some of this organic material
63 by bacterial activity led to the enhanced consumption of oxygen in subsurface waters,
64 resulting in widespread oceanic anoxia to euxinia (anoxic and sulfidic conditions) on regional
65 to global scales (Jenkyns, 2010 and references therein). Due to extensive oxygen depletion in
66 the oceans, OAEs are commonly associated with biotic turnover and extinction events.
67 Constraining, in detail, the timing, sequence and magnitude of environmental, climate and
68 biological disruptions during past OAEs provides a unique opportunity to deconvolve the
69 complex interplay of the oceans and atmosphere during major climate perturbations. As such,
70 OAEs can provide useful constraints for understanding the impact of modern anthropogenic
71 activity on future climate.

72 Oceanic Anoxic Event 2 (OAE 2) spanning the Cenomanian–Turonian (C/T) boundary
73 and occurring ~94 million years ago (Ma) (Obradovich et al., 1993; Gradstein et al., 2012;
74 Meyers et al., 2012), was one of the most intense and spatially extensive of the Mesozoic
75 OAEs (Jenkyns, 2010). As for all of the OAE’s, OAE 2 is characterised by the widespread

76 deposition of black shales, although the lateral extent of deposition is poorly known,
77 particularly in the Indo-Pacific region. The global influence of OAE 2 is illustrated by abrupt
78 changes in carbon-isotope ($^{13}\text{C}/^{12}\text{C}$) stratigraphy, formulated as $\delta^{13}\text{C}$, across the C/T boundary
79 from biostratigraphically well-dated sedimentary sections (e.g. Scholle and Arthur, 1980;
80 Schlanger et al., 1987; Tsikos et al., 2004). Because photosynthetically produced carbon
81 preferentially incorporates lighter ^{12}C over heavier ^{13}C isotopes, the anomalously high burial
82 rate of organic matter led to a positive carbon-isotope excursion (CIE) in marine and
83 atmospheric carbon reservoirs (Scholle and Arthur, 1980). The resultant 2–4 ‰ positive
84 excursion, registered in both carbonate and organic-carbon archives, is widely referred to as
85 the ‘OAE 2 CIE’ or ‘C/T CIE’ and provides an important chemostratigraphic tool for
86 identifying the event in sedimentary records (e.g. Scholle and Arthur, 1980; Tsikos et al.,
87 2004; Li et al., 2006; Jenkyns, 2010; Jenkyns et al., 2017).

88 The $\delta^{13}\text{C}$ profiles from OAE 2 sites are often correlated to the biostratigraphically well-
89 characterised and stratigraphically expanded section of semi-lithified chalk, originating from
90 foraminiferal–nannofossil ooze, exposed in the cliffs at Eastbourne, in southern England
91 (Fig. 1a) (Tsikos et al., 2004). General characteristics of the Eastbourne $\delta^{13}\text{C}$ curve include a
92 relatively sharp initial increase, a trough, a second peak, and an irregular plateau followed by
93 a gradual decrease to pre-excursion values (Fig. 1b). The rise and fall of $\delta^{13}\text{C}$ values has been
94 interpreted to reflect an increase and decrease in global carbon burial, respectively,
95 concomitant with the expansion and retreat of oceanic anoxia (e.g. Kuypers et al., 2002;
96 Jenkyns et al., 2017). OAE 2 was probably triggered by a massive injection of CO_2 into the
97 ocean-atmosphere system through extensive volcanism (Turgeon and Creaser, 2008; Du
98 Vivier et al., 2014; Scaife et al., 2017), which may have been superimposed on Earth’s natural
99 CO_2 cycles related to variations in Earth’s orbit around the sun (Fischer, 1986). The addition

100 of isotopically light C from volcanic sources may also have influenced the shape of the $\delta^{13}\text{C}$
101 curve (Jenkyns, 2010; Clarkson et al., 2018).

102 The trough in the $\delta^{13}\text{C}$ curve of OAE 2 correlates broadly with the so-called ‘Plenus
103 Cold Event’ (PCE), which in Eastbourne is characterised by the southward invasion of cool-
104 water boreal fauna into lower latitudes (Gale and Christensen, 1996). The occurrence of
105 boreal fauna occurred as two pulses, also defined by a rise in bulk oxygen-isotope values, and
106 is coincident with the location of the carbon-isotope trough. However, the stratigraphically
107 lowest occurrence of these cool-water indicators marking the onset of the PCE occurs below
108 the $\delta^{13}\text{C}$ trough. The PCE or ‘Benthic Oxidic Event’, as it is known locally, is now widely
109 recognised as a distinct period of cooling at a number of latitudes across the northern
110 hemisphere (e.g. Sinninghe Damsté et al., 2010), which can be linked to widespread re-
111 oxygenation and temporarily decreased silicate weathering. Evidence for re-oxygenation is
112 both geochemical, in terms of abrupt changes in redox-sensitive trace-element concentrations
113 and isotopic compositions (e.g. Dickson et al., 2016; Jenkyns et al., 2017; Clarkson et al.,
114 2018; Sweere et al., 2018) and biological, in terms of sea-floor colonisation by benthic
115 foraminifera (Eicher and Worstell, 1970; Kuhnt et al., 2005; Prokoph et al., 2013). Further,
116 tentative evidence for decreased silicate weathering, against a backdrop of an overall increase
117 over the OAE 2 interval, is derived from the lithium-isotope record from Eastbourne (Pogge
118 von Strandmann et al., 2013; Clarkson et al., 2018). The PCE thus represents a short-term
119 episode of re-oxygenation of the oceans with associated global cooling. This episode of re-
120 oxygenation is credited with temporarily decreasing global carbon burial and caused less
121 preferential extraction of ^{12}C from the ocean-atmosphere system, possibly causing the trough
122 in carbon-isotope values at this time, as registered in numerous northern hemisphere sections
123 (e.g. Tsikos et al., 2004; Kuhnt et al., 2005; Sageman et al., 2006; Hasegawa et al., 2010;
124 Jenkyns et al., 2017).

125 During OAE 2, the deposition of black shales probably started at marginal regions of
126 the southern North Atlantic and the Western Interior Seaway (WIS) in North America and
127 spread to the northern North Atlantic and eastward to the Tethys Ocean (Kuroda and
128 Ohkouchi, 2006). Previous studies have therefore focused on sites in these northern
129 hemisphere areas that show geochemical and sedimentological evidence for local and regional
130 anoxia and euxinia (e.g. Schlanger et al., 1987; Kuypers et al., 2002; Tsikos et al., 2004;
131 Kuhnt et al., 2005; Sageman et al., 2006; Jenkyns et al., 2007). However, carbon-isotope
132 records that potentially record a global signal may be modified by local or regional processes
133 such as upwelling, changes in the composition of planktonic biota, and diagenesis.
134 Consequently, global coverage of $\delta^{13}\text{C}$ stratigraphies, based on a multitude of records from
135 different ocean basins, is needed to constrain how carbon cycle perturbations during OAE 2
136 were expressed globally across the entire ocean-atmosphere system. High-resolution $\delta^{13}\text{C}$
137 stratigraphy is also fundamental for integrating palaeontological or more novel geochemical
138 data into a global carbon cycle framework. Presently, there are only a few isolated records
139 from the southern hemisphere, which compromises global-scale interpretations of OAE 2 (Li
140 et al., 2006; Navarro-Ramirez et al., 2016, 2017; Dickson et al., 2017; Li et al., 2017).

141 Here, we build on previously reported low-resolution $\delta^{13}\text{C}$ data from two palaeo-Pacific
142 sections located in New Zealand (Hasegawa et al., 2013). We present highly resolved
143 magnetic susceptibility (MS), total organic-carbon (TOC) and organic $\delta^{13}\text{C}$ ($\delta^{13}\text{C}_{\text{TOC}}$)
144 stratigraphies of the OAE 2 interval, the last of which is largely terrestrial in origin and
145 primarily monitors the carbon-isotope composition of atmospheric CO_2 . Correlation of the
146 carbon-isotope stratigraphies obtained here to a collection of globally dispersed carbon-
147 isotope records indicates a well-mixed ocean-atmosphere carbon system during OAE 2.
148 Detailed MS and TOC stratigraphies suggest dramatic changes in weathering regime and/or
149 intensity and, at least locally, a predominance of generally oxic conditions in the south-

150 western palaeo-Pacific Ocean. Finally, we take advantage of the high temporal resolution of
151 the $\delta^{13}\text{C}_{\text{TOC}}$ and MS records to produce a cyclostratigraphic age model. Together, these
152 datasets help constrain the timing, duration and character of OAE 2 from the unique
153 perspective of a marginal, southern Pacific Ocean setting with millennial-scale resolution.

154

155 **2. Stratigraphic Sections**

156 In this study, sedimentary sections exposed at Sawpit Gully (north-eastern South Island)
157 and Mangaotane Stream (eastern North Island) in New Zealand are examined (Fig. 1c). Both
158 sites have well-exposed and well-characterised sections spanning OAE 2 (Crampton et al.,
159 2001 and references therein; Hikuroa et al., 2009; Hasegawa et al., 2013). These OAE 2 strata
160 were deposited at a palaeolatitude of $\sim 70^\circ\text{S}$ (Sutherland, 1999) along the eastern continental
161 margin of the proto-New Zealand landmass at about the time of its separation from
162 Gondwanaland. Brief descriptions of the Sawpit Gully and Mangaotane sections are given
163 below, while a detailed description of each section is provided in the Supplementary Material
164 (SM).

165

166 *2.1 Sawpit Gully*

167 The Sawpit Gully section consists of non- or weakly calcareous siltstone, silty
168 sandstone, and sandstone, and finely disseminated pyrite appears sporadically throughout the
169 section. The OAE 2 sequence is mostly bioturbated. Although inoceramid bivalves are
170 abundant below and above the sampled section, there is a lack of macrofossils in the sampled
171 interval that indicates some disruption of the benthic ecosystem. The Sawpit Gully section
172 contains dinoflagellates (Schjøler and Crampton, 2014) but has not been examined further for
173 microfossils. Calcareous microfaunas, if present, are likely to be poorly preserved (Hasegawa

174 et al., 2013). The depositional environment of the Sawpit Gully section is poorly constrained,
175 but the lithology and stratigraphic context suggest mid- to outer shelf depths.

176

177 2.2 *Mangaotane B*

178 The Mangaotane B section at Mangaotane Stream is dominated by non- or weakly
179 calcareous, indurated mudstone, with minor siltstone and very fine sandstone. The section is
180 characterised by the presence of red shales. The red shales have previously been identified as
181 ‘Cretaceous Oceanic Red Beds’ (CORBs) deposited under oxic conditions (Hikuroa et al.,
182 2009). The red coloration is attributed to the presence of hematite (Fe_2O_3), which may have
183 developed diagenetically from hydroxide species formed in oxidising environments (e.g. Hu
184 et al., 2005; Hikuroa et al., 2009). There is an absence of macrofossils in the Mangaotane B
185 red shales, as is typical of CORBs, possibly due to their adaptation to preceding low-oxygen
186 conditions (Wang et al., 2009). The thickest of these ‘red-beds’ (28.6–44.6 m) is well exposed
187 in Mangaotane B (Fig. 2 and Fig. 3) and is not significantly disturbed by faulting. This major
188 red-bed unit is interbedded with four ‘green beds’ of up to 43 cm thick that are interpreted to
189 reflect anoxic conditions during deposition or early diagenesis (Lyle, 1983). The sequence is
190 mostly bioturbated and mottled to varying degrees, but contains fine remnant millimetre-scale
191 lamination in places and thin (<10 cm thick) laminated beds in the interval between 26 m and
192 the base of the main red-bed. Although common below and above the section, macrofossils
193 are lacking in the OAE 2 interval itself, indicating some disruption of the ecosystem. The
194 environment of deposition for Mangaotane B was likely to have been at upper slope depths of
195 ~300 m or greater (Crampton et al., 2001), which contrasts with the deeper pelagic
196 depositional environments that are typical of red shales from other marine sites. The
197 Mangaotane B section is located ~2 km northwest and downstream of the Mangaotane A
198 section, which exposes the same lithological units spanning OAE 2 but is structurally

199 complicated over the interval of OAE 2 (Hasegawa et al., 2013).

200

201 **3. Materials and Methods**

202

203 *3.1 Sample Collection*

204 Fieldwork was undertaken during three separate sampling trips between March, 2015
205 and February, 2016. Detailed stratigraphic sections spanning the OAE 2 interval were logged
206 and sampled at both the Sawpit Gully and Mangaotane B sites. In total, 662 samples were
207 taken from both exposures, with an average sampling resolution of 10 cm, using a concrete
208 cutter to remove blocks of rock arrayed along bedding-perpendicular transects (see SM for
209 details). This approach allowed for stratigraphically controlled, bulk sampling of relatively
210 unweathered material. In Sawpit Gully, 477 samples were collected, while in Mangaotane B,
211 185 samples were taken, in both cases along four non- or slightly overlapping transects (A–D)
212 (Fig. 4 and Fig. 5).

213

214 *3.2 Geochemical Analyses*

215 Values for TOC, $\delta^{13}\text{C}_{\text{TOC}}$, and MS were determined on every sample in the
216 Sawpit Gully (n = 477) and Mangaotone B (n = 185) composite stratigraphies (see SM for
217 details). Four samples dispersed throughout the Mangaotane B section (two grey shales and
218 two red shales) were analysed for their lithological components by X-ray diffractometry
219 (XRD). Rock-Eval pyrolysis was carried out on 6 samples from Sawpit Gully and 18 samples
220 from Mangaotane B to obtain TOC and carbonate content, as well as the T_{max} (the
221 temperature of maximum hydrocarbon generation from kerogens during pyrolysis) and HI

222 (hydrogen index; amount of hydrocarbons generated by pyrolysis at T_{\max} relative to TOC)
223 organic geochemistry values.

224

225 3.3 *Time-Series Analyses*

226 An orbitally calibrated age model was developed for Sawpit Gully based on the
227 frequency content of the $\delta^{13}\text{C}_{\text{TOC}}$ and MS profiles constrained by key features of these
228 records, including the start and end of the CIE (see SM for details).

229

230 4. Results and Discussion

231

232 4.1 *Origin of organic matter*

233 In a preceding study (Hasegawa et al., 2013), $\delta^{13}\text{C}_{\text{TOC}}$ records for OAE 2 were derived
234 for Sawpit Gully and Mangaotane B, albeit with low temporal resolution of ~50 ky. These
235 records provide good first-order constraints on the character of OAE 2 along the palaeo-
236 continental margin of New Zealand and show clear evidence for a positive CIE, but lack
237 sufficient resolution to allow for global correlation and identification of shorter duration
238 phenomena, such as the $\delta^{13}\text{C}$ trough coincident with the PCE. The highly resolved sampling
239 interval of 10 cm of this study corresponds to a temporal resolution of approximately 1–3 ky
240 in Sawpit Gully and 4–8 ky in Mangaotane B, using the plausible 500–900 ky duration for
241 OAE 2, defined as the entire CIE from the onset to return to pre-excursion values, as
242 identified previously (Sageman et al., 2006; Meyers et al., 2012; Ma et al., 2014; Li et al.,
243 2017; Jones et al. 2019).

244 In both the Sawpit Gully and Mangaotane B sections, TOC concentrations (<0.1 wt %)
245 are approximately two orders of magnitude lower than typically observed in OAE 2 black
246 shales of the northern hemisphere (Fig. 3 and Fig. 6), where wt % TOC values of up to 30–
247 50 % have been documented that are indicative of locally persistent anoxic or euxinic
248 conditions (Kuhnt et al., 2005; Kuypers et al., 2002; Monteiro et al., 2012; Tsikos et al.,
249 2004). Such low TOC concentrations in the Sawpit Gully and Mangaotane B sections instead
250 suggest relatively well-oxygenated depositional environments along the continental margin of
251 New Zealand, in which preserved organic matter rarely exceeds 0.5 % in the sediment (e.g.
252 Arthur and Sageman, 1994). The deposition of oceanic red beds, including the CORBs of
253 Mangaotane B, and the presence of bioturbation in both New Zealand sections, also indicate
254 mostly oxic conditions during deposition (e.g. Hu et al., 2005). It is possible that this is a
255 consequence of shallow depositional environments of mid to outer shelf depths in the
256 Sawpit Gully section. By contrast, the Mangaotane B section was deposited at depths of
257 ~300 m or greater (Crampton et al., 2001), indicating well-oxygenated environments at
258 intermediate depths in the palaeo-South Pacific Ocean during OAE 2.

259 Despite a dominantly oxic depositional setting, the minor green beds that occur
260 irregularly within the major red-bed of Mangaotane B are inferred to have developed under
261 reducing conditions at or below the sea floor, where red Fe^{3+} was reduced to green Fe^{2+} (Lyle,
262 1983), suggestive of intermittent low-oxygen conditions during deposition. Areas of remnant
263 lamination throughout the section, but not in red shales, also suggest fleeting intervals of
264 oxygen-deprived conditions during which bioturbators could not occupy the sediment. In
265 summary, all indicators point toward generally oxic conditions with temporarily more
266 oxygen-deprived phases during the deposition of OAE 2 sediments along the continental
267 margin of New Zealand.

268 Organic geochemical indicators imply that the organic matter from the Sawpit Gully
269 section is primarily of terrestrial origin (Fig. 7) and as such, is mostly derived from
270 atmospheric CO₂ (Hasegawa et al., 2013). Therefore, the Sawpit Gully $\delta^{13}\text{C}_{\text{TOC}}$ record is
271 expected to represent carbon-isotope fluctuations of the atmospheric CO₂ reservoir and
272 accurately record global changes in the carbon cycle. In addition, MS values are relatively
273 uniform in the Sawpit Gully section (Fig. 6), with the exception of two prominent maxima
274 that correspond with relatively low TOC. Magnetic Susceptibility is interpreted to track
275 changes in weathering regime and/or intensity (e.g. Ellwood et al., 2000; Li et al., 2017) due
276 to the association of magnetic minerals with terrestrial material. Therefore, the relatively
277 invariant MS record for large parts of the Sawpit Gully section indicates that the character
278 and/or flux of weathered material, carrying terrestrial carbon from the continent into the
279 oceans, is likely to have been relatively consistent throughout OAE 2 at this location.

280 Although the Sawpit Gully $\delta^{13}\text{C}_{\text{TOC}}$ record is expected to record carbon-isotope
281 fluctuations of the global atmospheric CO₂ reservoir, interpretation of the Mangaotane B
282 $\delta^{13}\text{C}_{\text{TOC}}$ stratigraphy is more complex. Below the major red-bed (<28.6 m), TOC and MS
283 values are similar to those for Sawpit Gully, and organic geochemical and petrographic
284 markers indicate that organic matter from the lower part of the Mangaotane B section is
285 primarily of terrestrial origin (Hasegawa et al., 2013). Therefore, the $\delta^{13}\text{C}_{\text{TOC}}$ record for the
286 interval leading up to red-bed deposition at Mangaotane B is interpreted to reflect global
287 variability in $\delta^{13}\text{C}$, and changes in the isotopic composition of the atmospheric carbon
288 reservoir.

289 However, low TOC coincident with persistently high MS values characterise the major
290 red-bed interval (28.6–44.6 m), which produces a stratigraphy that differs from that of
291 Sawpit Gully (Fig. 3). Higher MS values, coincident with the lowest concentrations of
292 preserved organic matter, indicate that a higher proportion and/or a different type of

293 lithogenic material was transported to this location on the New Zealand margin. Hasegawa et
294 al. (2013) observed a reduction in organic-carbon and terrestrial kerogen concentrations,
295 coupled with a decline in $\delta^{13}\text{C}_{\text{TOC}}$ values, in a correlative stratigraphic unit within the adjacent
296 Mangaotane A section. These authors argued for a reduction in the proportion of organic
297 matter sourced from terrestrial plants in the bulk sediment when TOC values are low, shifting
298 the net $\delta^{13}\text{C}_{\text{TOC}}$ signature towards the lighter compositions of marine organic matter. Although
299 T_{max} and HI could not be measured at Mangaotane B because of exceedingly low TOC
300 contents below instrumental detection limits, given the close proximity of the two
301 Mangaotane sections, the organic geochemistry indices of the Mangaotane A red-bed are
302 considered to be directly applicable to the red-bed of Mangaotane B. Thus, we infer that
303 variable mixing of marine and terrestrially derived organic matter in the upper part of the
304 Mangaotane B section within the major red-bed likely obscures the global carbon-isotope
305 signature, which is superimposed on the changes in global carbon cycling.

306

307 4.2 $\delta^{13}\text{C}_{\text{TOC}}$ stratigraphy for Sawpit Gully and Mangaotane B: Global versus local 308 signatures

309 The character of the Sawpit Gully and Mangaotane B $\delta^{13}\text{C}_{\text{TOC}}$ stratigraphies differ
310 considerably within the CIE interval defining the OAE 2 proper. While palynofloras support
311 overall correlations to the C/T boundary (Hasegawa et al., 2013), they do not allow for
312 detailed, independent correlations within the CIE interval between the Sawpit Gully and
313 Mangaotane B sections. However, both sites show a clear 2 ‰ positive $\delta^{13}\text{C}_{\text{TOC}}$ excursion at
314 the start of the interval away from pre-excursion values of -25 ‰, followed by a return to pre-
315 excursion values at the end of the CIE (Fig. 8). The onset of the CIE in both independent
316 sections is abrupt, and the replication between the two sites suggests that stratigraphic
317 condensation is minimal, but cannot be entirely ruled out. A trough superimposed on the

318 beginning of the positive CIE can be seen in both sections (red band in Fig. 8) but is more
319 pronounced in Mangaotane B (Minimum 1) than in Sawpit Gully. When both New Zealand
320 sections are compared to the Eastbourne $\delta^{13}\text{C}_{\text{carb}}$ stratigraphy, the timing of this trough in the
321 early phase of OAE 2 appears to coincide with that of the PCE, which previously has not been
322 well documented in the southern hemisphere. The small rise in $\delta^{13}\text{C}_{\text{TOC}}$ within the trough in
323 the Sawpit Gully section possibly separates the two pulses of the PCE recorded in other
324 proxies elsewhere in the northern hemisphere (Jenkyns et al., 2017). It is noteworthy that MS
325 values increase in both sections just after the PCE, at the onset of the CIE plateau, possibly
326 indicating a change in weathering regime and/or weathering intensity related to warmer
327 climates after a period of cooling.

328 The remaining part of the Sawpit Gully stratigraphy above the stratigraphic expression
329 of the PCE resembles the classically defined OAE 2 section in Eastbourne (Fig. 8). By
330 contrast, the $\delta^{13}\text{C}_{\text{TOC}}$ stratigraphy for Mangaotane B shows two additional minima, both of
331 large amplitude, displaying shifts of ~ 3 and ~ 5 ‰ towards more negative values for
332 Minimum 2 and Minimum 3, respectively (Fig. 3). Such extreme negative shifts are not
333 typical for other OAE 2 sections, although negative excursions in the ‘plateau’ phase have
334 been recorded in $\delta^{13}\text{C}_{\text{carb}}$ records from the Central European shelf sea, possibly related to the
335 elevated presence of isotopically light carbon in bottom waters (Voigt et al., 2007, 2008). In
336 the Mangaotane B stratigraphy, Minima 2 and 3 also correlate with anomalously low TOC
337 contents (see SM for details). As discussed in section 4.1, these offsets are possibly caused by
338 variable mixing of marine and terrestrially derived organic matter that obscures the global
339 carbon-isotope signatures, as Cretaceous marine organic matter generally had a more negative
340 carbon-isotope signature than contemporaneous terrestrial organic matter, likely due to
341 elevated atmospheric CO_2 levels relative to today (e.g. Dean et al., 1986; Hayes et al., 1999).
342 Alternatively, these minima could be the result of variable mixing between different terrestrial

343 sources of organic matter with differing $\delta^{13}\text{C}_{\text{TOC}}$. Carbon-isotope values are variable within
344 terrestrial higher plants (Gröcke, 2002), so that Minima 2 and 3 could be explained by an
345 elevated proportion of terrestrial organic matter with a relatively low $\delta^{13}\text{C}_{\text{TOC}}$ signature, as is
346 the case for OAE 2 black shales in Italy (Farrimond et al., 1990; Kuroda et al., 2007).
347 Regardless, the potential combination of changing organic matter provenance and diminished
348 instrumental accuracy associated with low C concentrations during Minima 2 and 3 indicate
349 that this part of the Mangaotane stratigraphy will likely mask global $\delta^{13}\text{C}$ variations. To
350 facilitate comparison of the Mangaotane B $\delta^{13}\text{C}_{\text{TOC}}$ stratigraphy with globally distributed
351 records, only samples with >0.1 wt % TOC were considered to have reliable carbon-isotope
352 values. Filtering the $\delta^{13}\text{C}_{\text{TOC}}$ dataset in this manner removes Minima 2 and 3 from the
353 Mangaotane B $\delta^{13}\text{C}_{\text{TOC}}$ record, but Minimum 1 is still visible (curve E in Fig. 8). Importantly,
354 the screened $\delta^{13}\text{C}_{\text{TOC}}$ record, including those for the lower part of the Mangaotane B section
355 below the major red-bed, no longer show a systematic relationship with TOC content and the
356 $\delta^{13}\text{C}_{\text{TOC}}$ record resembles the Sawpit Gully curve. Thus, only the filtered carbon-isotope
357 record for Mangaotane B is interpreted to represent global $\delta^{13}\text{C}_{\text{TOC}}$ signatures and is
358 considered for the remainder of the discussion. Following screening, the exact termination of
359 the PCE trough and the beginning of the decrease to pre-excursion values cannot be
360 determined with absolute certainty in the Mangaotane B $\delta^{13}\text{C}_{\text{TOC}}$ record.

361 It is conceivable that the $\delta^{13}\text{C}_{\text{TOC}}$ values for Sawpit Gully have also been influenced by
362 local variations, including the source of organic matter, although to a much lesser extent than
363 in Mangaotane B due to order-of-magnitude higher TOC contents. For example, the small
364 positive excursion of ~ 0.5 ‰ at the base of the Sawpit Gully section (~ 1.0 m) and the
365 associated increase in wt % TOC could be the result of an elevated input of terrestrial organic
366 matter with a relatively positive $\delta^{13}\text{C}_{\text{TOC}}$. Such minor fluctuations, however, have no
367 significant effect on the general characteristics of the Sawpit Gully curve and do not influence

368 the overall interpretation of the $\delta^{13}\text{C}_{\text{TOC}}$ record in the context of changes to the atmospheric
369 CO_2 and hence the global ocean–atmosphere carbon reservoir during OAE 2.

370

371 4.3 $\delta^{13}\text{C}_{\text{TOC}}$ stratigraphy for Sawpit Gully and Mangaotane B: Low versus high resolution

372 Both the Sawpit Gully and Mangaotane B $\delta^{13}\text{C}_{\text{TOC}}$ datasets of this study are in good
373 agreement with the previous results for the same localities (Hasegawa et al., 2013) regarding
374 their general OAE 2 profiles. However, the new Mangaotane B and Sawpit Gully $\delta^{13}\text{C}_{\text{TOC}}$
375 curves have greatly improved temporal resolution. Most importantly, when examined in
376 detail, the high-resolution $\delta^{13}\text{C}_{\text{TOC}}$ records presented here reveal additional higher frequency
377 oscillations that are not apparent in the lower resolution chemostratigraphy. For example, the
378 Hasegawa et al. (2013) curves do not capture the abruptness of the onset of the CIE, nor the
379 trough that correlates with the PCE. These features demonstrate the importance of high-
380 resolution sampling for capturing the full characteristics of the $\delta^{13}\text{C}_{\text{TOC}}$ stratigraphy, hence
381 facilitating global correlation.

382 The carbon-isotope expression of the trough related to the PCE in both New Zealand
383 sections is noteworthy (Fig. 3, Fig. 6 and Fig. 8). While the carbon-isotope expression of the
384 PCE is readily identified in the northern hemisphere (Fig. 8), the New Zealand margin
385 represents one of only three regions in the southern hemisphere where its signature can be
386 identified, the others being the southern Tibet section of Gongzha formerly situated in the
387 southern hemisphere at $\sim 35^\circ\text{S}$ (curve H in Fig. 8; Li et al., 2017) and, tentatively, the
388 Peruvian Western Platform (curve G in Fig. 8; Navarro-Ramirez et al., 2016, 2017). Previous
389 studies have not, however, formally correlated the $\delta^{13}\text{C}$ trough with this cooling and
390 reoxygenation event. Identification of the PCE interval in both New Zealand sections
391 confirms the assumption that these southern high latitudes record global changes in the carbon

392 cycle, but without accompanying palaeotemperature data, the occurrence of ocean–
393 atmosphere cooling cannot be demonstrated.

394

395 4.4 *Astronomical constraints on the timing, duration and character of OAE 2*

396 The $\delta^{13}\text{C}_{\text{TOC}}$ stratigraphy from Sawpit Gully has a sufficiently high resolution to reveal
397 prominent high-frequency cycles that are superimposed on the OAE 2 CIE curve. Spectral
398 analysis reveals a significant wavelength of 3.9 m with respect to stratigraphic thickness that
399 exceeds the 95 % confidence level in the Sawpit Gully $\delta^{13}\text{C}_{\text{TOC}}$ record (Fig. 9a; see SM for
400 details). To this end, time-series analysis was conducted to characterise these cycles and
401 determine whether astronomical forcing was a potential driver of the observed changes in
402 $\delta^{13}\text{C}_{\text{TOC}}$ and whether these cycles could be used to determine the duration of the CIE as
403 recorded in the section.

404 The Sawpit Gully section does not contain any fauna or lithological indicators that can
405 be used to independently constrain the timing and duration of OAE 2. Therefore, the $\delta^{13}\text{C}_{\text{TOC}}$
406 dataset for Sawpit Gully was instead correlated to an equally resolved carbonate $\delta^{13}\text{C}$ OAE 2
407 section from Gongzha, Tibet that was situated in the southern hemisphere at $\sim 35^\circ\text{S}$ during the
408 mid-Cretaceous (Li et al., 2017) (Fig. 6). For the Tibetan section, an orbital timescale was
409 constructed from an eccentricity-paced MS record (Li et al., 2017). This correlation (Fig. 6)
410 provides approximate ages for the onset (94.55 Ma at 4.71 m) and end (93.73 Ma at 37.89 m)
411 of the CIE in the Sawpit Gully stratigraphy. These age constraints were used to create a linear
412 age model and convert the $\delta^{13}\text{C}_{\text{TOC}}$ record to the time domain. A simple calculation of the
413 sediment thickness of the excursion (33.18 m) divided by the cycle length (3.9 m) indicates
414 that 8.5 cycles can be accommodated within the excursion. We hypothesise that the 3.9 m
415 cycles are paced with short eccentricity (100 ky), indicating a minimum duration of ~ 850 ky
416 for the $\delta^{13}\text{C}_{\text{TOC}}$ excursion from the onset to return to pre-excursion values (8.5 cycles x

417 100 ky), which agrees with the upper estimates of 820 ± 25 ky (Li et al., 2017) and 866
418 ± 19 ky (Sageman et al., 2006) previously reported for the duration of the OAE 2 CIE (see
419 SM for details).

420 To test the hypothesis that the 3.9 m cycle corresponds to eccentricity, the age-corrected
421 $\delta^{13}\text{C}_{\text{TOC}}$ record was band-pass filtered with a filter centred at 0.01/ky (100 ky) and a
422 bandwidth of 0.003/ky (77–143 ky). The amplitude variations of the $\delta^{13}\text{C}_{\text{TOC}}$ dataset were
423 compared with the orbital reference record of eccentricity (Laskar et al., 2004), which was
424 filtered to extract the short (100 ky) eccentricity cycle using the same parameters as the
425 carbon-isotope record. To achieve the best correlation of the filtered $\delta^{13}\text{C}_{\text{TOC}}$ record with the
426 100 ky eccentricity cycle, the age of the end of the CIE was adjusted from 93.73 Ma to
427 93.62 Ma (age-shift of 110 ky), which resulted in a one-to-one correlation with the filtered
428 record. The weak short eccentricity cycles between 94.3 Ma and 93.9 Ma likely resulted in
429 weak pacing of the carbon cycle at this time, which gave rise to the poorly developed cycles
430 observed in the $\delta^{13}\text{C}_{\text{TOC}}$ record. Uncertainties are estimated as one eighth of an eccentricity
431 cycle (12.5 ky) per data point due to the error from comparison with the orbital reference
432 record.

433 Spectral analyses of the MS record were also conducted to test the age model derived
434 from $\delta^{13}\text{C}_{\text{TOC}}$ data (see SM for details). As MS is interpreted to represent variations in the
435 style and/or intensity of weathering input into the marine environment, it is also expected to
436 record orbital cycles (Ellwood et al., 2008) that are more prominent in high-latitude records
437 (Fischer, 1986), such as the palaeo-south Pacific region of our study sites. After applying the
438 age model established from the $\delta^{13}\text{C}_{\text{TOC}}$ record, spectral analysis revealed obliquity (38 ky)
439 and precession (21 ky) cycles above the 95% threshold in the age-corrected MS dataset
440 (Fig. 9b). Numerical calculations indicate that obliquity has slowed since the Cretaceous
441 because of tidal dissipation, resulting in the observed 38 ky cycle compared to the modern-

442 day frequency of 41 ky (Laskar et al., 2004). The precise obliquity solution (i.e. temporal
443 accuracy of cycles) is not accurate beyond 65 Ma because of the chaotic evolution of the
444 planetary orbits, but the calculated obliquity frequency of cycles should be robust (Laskar et
445 al., 2004, 2011).

446 The identification of eccentricity cycles in the Sawpit Gully $\delta^{13}\text{C}_{\text{TOC}}$ record, as well as
447 the appearance of obliquity and precession cycles in the MS record for the same section, gives
448 confidence in the robustness of the resultant age model and its ability to constrain the timing
449 and duration of specific events and excursions within OAE 2. On this basis, the position of the
450 Cenomanian-Turonian boundary, nominally dated at 93.9 Ma; (Obradovich et al., 1993;
451 Gradstein et al., 2012; Meyers et al., 2012), could be placed in the second half of the CIE
452 plateau at 27.96 m in the Sawpit Gully $\delta^{13}\text{C}_{\text{TOC}}$ stratigraphy (Fig. 6). This position contrasts
453 with the placement of the C/T boundary based on available dinoflagellate biostratigraphy
454 between ~1.9 m and ~16.5 m (Hasegawa et al., 2013). The orbitally tuned age model for the
455 Sawpit Gully $\delta^{13}\text{C}_{\text{TOC}}$ record also implies that the duration of the CIE associated with OAE 2
456 was at least 930 ± 25 ky, which is only slightly longer than the upper estimate of 866 ± 19 ky
457 determined previously for the Western Interior Seaway of North America (Sageman et al.,
458 2006). This duration corresponds to a temporal sampling resolution of ~3 ky in Sawpit Gully
459 and ~9 ky in Mangaotane B. The Sawpit Gully record indicates that the onset of the carbon-
460 isotope trough related to the PCE occurred approximately 30 ± 13 ky after the onset of the
461 CIE. This contrasts with the estimate of Li et al. (2017), who placed the trough 110 ± 25 ky
462 after the CIE onset. This apparent discrepancy could be the result of potential stratigraphic
463 condensation of the Sawpit Gully record. The Sawpit Gully dataset further implies that the
464 PCE carbon-isotope trough lasted for at least 200 ± 25 ky and that the CIE plateau phase
465 persisted for 660 ± 25 ky, thereafter recovering to background $\delta^{13}\text{C}_{\text{TOC}}$ values over 40
466 ± 25 ky. These constraints contrast with those reported in Li et al. (2017), who estimated

467 durations of 80 ± 25 ky for the carbon-isotope trough related to the PCE, 370 ± 25 ky for the
468 plateau phase and 170 ± 25 ky for the subsequent recovery to background levels. If it is
469 assumed that the age model presented here can be reliably extrapolated to the pre-OAE 2
470 interval, then the observed shift towards more negative $\delta^{13}\text{C}_{\text{TOC}} \sim 50$ ky prior to the onset of
471 the event is broadly consistent with the onset of Large Igneous Province activity (Du Vivier et
472 al., 2015) and might therefore be related to the injection of isotopically light C into the
473 atmosphere.

474 Despite the warm equable climates of the greenhouse world during OAE 2, the global
475 temperature regime most likely responded to changes in solar insolation driven by orbital
476 cycles (e.g. Meyers et al., 2001; Dickson et al., 2017; Li et al., 2017). The concomitant
477 changes in weathering and nutrient input would have led to varying rates of organic matter
478 burial at low latitudes and corresponding global carbon-isotope variability forced by
479 eccentricity. The detection of eccentricity cycles in the $\delta^{13}\text{C}_{\text{TOC}}$ record in Sawpit Gully
480 supports this inference. The recording of obliquity cycles in the MS data suggests that
481 changes in insolation driven by astronomical forcing in the high latitudes of the south Pacific
482 had a direct impact on changes in weathering regime and/or intensity along the New Zealand
483 continental margin (Fischer, 1986).

484

485 4.5 *Correlation of the Sawpit Gully and Mangaotane B $\delta^{13}\text{C}_{\text{TOC}}$ stratigraphy with other* 486 *records*

487 Fig. 8 shows the $\delta^{13}\text{C}_{\text{TOC}}$ stratigraphy for Sawpit Gully and Mangaotane B in
488 comparison to the C-isotope datasets of other well-defined OAE 2 sections from the former
489 north European epicontinental pelagic shelf sea (Eastbourne, UK; Tsikos et al., 2004), eastern
490 edge of the proto-Atlantic Ocean (Tarfaya Basin, Morocco; Kuhnt et al., 2005), Western

491 Interior Seaway (Colorado, USA; Sageman et al., 2006) and palaeo-Pacific Ocean (Tappu,
492 Japan; Hasegawa et al., 2010) in the northern hemisphere, as well as sections deposited in the
493 southern hemisphere (Western Platform, Peru; Navarro-Ramirez et al., 2016, 2017; and
494 Gongzha, Tibet; Li et al., 2017). Correlation of the new Sawpit Gully and Mangaotane B
495 $\delta^{13}\text{C}_{\text{TOC}}$ datasets with other carbon-isotope stratigraphies is based on a combination of
496 biostratigraphy, where applicable, and the location of prominent carbon-isotope shifts and
497 $\delta^{13}\text{C}_{\text{TOC}}$ maxima/minima that are present in the classically defined Eastbourne section (Tsikos
498 et al., 2004).

499 All of the above carbon-isotope stratigraphies show the characteristic phases of OAE 2
500 enabling robust correlation of the New Zealand sections to OAE 2 sections from other parts of
501 the world. The fact that the global carbon perturbation associated with OAE 2 is recorded in
502 different archives, including terrestrial organic matter, marine organic matter and carbonates
503 of both deep (pelagic) and shallow-water origin (Fig. 8), is a strong indication that the ocean–
504 atmosphere inorganic carbon system was well mixed at this time. However, even though all of
505 the above sections display similar general characteristics, each curve differs markedly in its
506 higher frequency features. For example, while the curves from Tarfaya (Morocco), Colorado
507 (USA) and the Western Platform (Peru) show C-isotope background levels consistent with
508 those of marine organic matter ($\delta^{13}\text{C}_{\text{TOC}}$ values of -27 to -29 ‰; Dean and Arthur, 1987), the
509 records from Sawpit Gully, Mangaotane B and Tappu have background values approximately
510 consistent with those of terrestrial organic matter ($\delta^{13}\text{C}_{\text{TOC}}$ values of -23 to -25 ‰; Dean and
511 Arthur, 1987). These differing carbon-isotope baseline values reflect local differences in their
512 respective organic-carbon sources. Furthermore, the positive CIEs representing the OAE 2
513 proper vary in magnitude. This phenomenon might be due to local variations in the carbon-
514 cycle response, induced by locality-dependent fluctuations in productivity, the source of
515 organic matter, and/or diagenetic alteration.

516 The OAE 2 records from New Zealand indicate that oxic conditions were most likely
517 prevalent at mid- to high latitudes, at least locally, along the southwest Pacific margin on the
518 upper continental slope during OAE 2. Records of OAE 2 from Japan, USA and Peru indicate
519 that similarly oxic conditions are likely to have been present in the mid- to high latitudes of
520 the northwest and northeast Pacific and the sub-equatorial eastern Pacific, whereas conditions
521 were likely anoxic in at least the mid-depth waters of the equatorial Pacific Ocean under areas
522 of upwelling at this time, as shown by the organic-rich sedimentary record, particularly on
523 submarine volcanic plateaus (Schlanger and Jenkyns, 1976; Arthur et al., 1987; Schlanger et
524 al., 1987; Takashima et al., 2011). These observations are in agreement with an Earth system
525 model, which suggests oxic conditions in the water column and seafloor of the south-western
526 and north-western Pacific Oceans (Monteiro et al., 2012). Despite apparently oxygen-rich
527 conditions, the partial collapse of benthic ecosystems in New Zealand and Japan indicates that
528 major environmental perturbations occurred before and/or during OAE 2. Deconvolving the
529 cause of this paradox will be the focus of future studies.

530

531 **5. Conclusions**

532 We present the first high-resolution carbon-isotope stratigraphy from the high
533 southern latitude palaeo-South Pacific Ocean during the warm, ‘super-greenhouse’ oceanic
534 anoxic event spanning the Cenomanian/Turonian boundary at ~94 Ma (OAE 2). To this end,
535 $\delta^{13}\text{C}_{\text{TOC}}$ datasets have been acquired with an unprecedented temporal resolution of 3 ky and
536 9 ky for two outcrops at Sawpit Gully and Mangaotane B, respectively, in the New Zealand
537 sector of the palaeo-Pacific Ocean. These new $\delta^{13}\text{C}_{\text{TOC}}$ records are based primarily on
538 terrestrial organic matter and hence are expected to represent carbon-isotope fluctuations of
539 the atmospheric CO_2 reservoir and accurately record global changes in the carbon cycle. Both
540 sections show the characteristic chemostratigraphic phases of OAE 2, such as the initial ~2 ‰

541 excursion in $\delta^{13}\text{C}$ marking the onset of the CIE, and the transient shift towards lower $\delta^{13}\text{C}$
542 values that correlates with the PCE. These distinctive features enable robust correlation of the
543 New Zealand sections to OAE 2 sections from other parts of the world, irrespective of the
544 type of archive, which indicates a globally well-mixed ocean–atmosphere carbon system
545 during OAE 2.

546 The high-resolution carbon-isotope stratigraphy for the Sawpit Gully section
547 furthermore enables an astronomical age model to be established for this record based on
548 cyclic oscillations, permitting the dating of specific perturbations of the carbon cycle within
549 the $\delta^{13}\text{C}_{\text{TOC}}$ record. An approach based on cyclic oscillations in the carbon-isotope dataset was
550 used for orbital calibration. This astronomical age model suggests a duration of 930 ± 25 ky
551 for the primary CIE associated with OAE 2, agreeing with estimates from the Western
552 Interior of North America. Further, this model implies a minimum duration of 200 ± 25 ky for
553 the PCE, beginning 30 ± 13 ky after the initial onset of the CIE. The lithologies and ultra-low,
554 sub-percent level TOC contents of the New Zealand sites implies that oxic conditions were
555 developed, at least locally, along the palaeo-Pacific Ocean margins at mid- to high latitudes
556 during OAE 2, while conditions were likely anoxic in mid-depth waters of the equatorial
557 oceans at this time. The major red-bed present in the Mangaotane B section is inferred to
558 record dramatic changes in weathering regime and/or intensity so that other environmental
559 perturbations, in addition to changing redox-conditions, may have given rise to a unique
560 environmental response to OAE 2 in the high-latitude south Pacific region.

561

562 **Acknowledgements**

563 The authors gratefully acknowledge the Royal Society of New Zealand Marsden Fund
564 (UOO1314) and a University of Otago Doctoral Scholarship for financial support. We also
565 thank Bradley Sageman and an anonymous reviewer for their valuable comments that helped

566 improve the manuscript. We thank the Murray family at Bluff Station for access to
567 Sawpit Gully and the trustees of the Mangaotane Trust for access to Mangaotane Valley. We
568 are also grateful to Michael Hannah, Ben Hines and Wiremu Wells for help with fieldwork.
569 We thank Rachael Baxter for assistance with sample preparation David Mucchiarone for
570 assistance with carbon analyses and Gemma Kerr for assistance with XRD measurements.
571 Supplementary material related to this article can be found online.

572

573 **References**

- 574 Arthur, M., Schlanger, S., Jenkyns, H., 1987. The Cenomanian-Turonian Oceanic Anoxic
575 Event, II. Palaeoceanographic controls on organic-matter production and preservation.
576 In: Brooks, J, Fleet, A.J. (Eds) Marine Petroleum Source Rocks, Geol. Soc., London,
577 Special Publication 26, 401–420.
- 578 Arthur, M.A., Sageman, B.B., 1994. Marine shales: depositional mechanisms and
579 environments of ancient deposits. *Annu. Rev. Earth Planet. Sci.* 22, 499–551.
- 580 Clarkson, M.O., Stirling, C.H., Jenkyns, H.C., Dickson, A.J., Porcelli, D., Moy, C.M., Pogge
581 von Strandmann, P.A.E., Cooke, I.R., Lenton, T.M., 2018. Uranium isotope evidence
582 for two episodes of deoxygenation during Oceanic Anoxic Event 2. *Proc. Natl. Acad.*
583 *Sci.* 115, 2918–2923.
- 584 Crampton, J., Raine, I., Strong, P., Wilson, G., 2001. Integrated biostratigraphy of the
585 Raukumara Series (Cenomanian–Coniacian) at Mangaotane Stream, Raukumara
586 Peninsula, New Zealand. *N.Z. J. Geol. Geophys.* 44, 365–389.
- 587 Dean, W.E., Arthur, M.A., Claypool, G.E., 1986. Depletion of ^{13}C in Cretaceous marine
588 organic matter: Source, diagenetic, or environmental signal? *Mar. Geol.* 70, 119–157.
- 589 Dean, W., Arthur, M., 1987. Inorganic and organic geochemistry of Eocene to Cretaceous
590 strata recovered from the lower continental rise, North American Basin, Site 603, Deep
591 Sea Drilling Project Leg 93. In: van Hinte, Wise, S.W., Jr et al., Initial Reports of the
592 Deep Sea Drilling Project, Washington (US Government Printing Office) 93, 1093–
593 1137.
- 594 Dickson, A.J., Jenkyns, H.C., Porcelli, D., van den Boorn, S., Idiz, E., 2016. Basin-scale
595 controls on the molybdenum-isotope composition of seawater during Oceanic Anoxic
596 Event 2 (Late Cretaceous). *Geochim. Cosmochim. Acta* 178, 291–306.

597 Dickson, A.J., Saker-Clark, M., Jenkyns, H.C., Bottini, C., Erba, E., Russo, F., Gorbanenko,
598 O., Naafs, B.D.A., Pancost, R.D., Robinson, S.A., Van den Boorn, S., Idiz, E., 2017. A
599 Southern Hemisphere record of global trace-metal drawdown and orbital modulation of
600 organic-matter burial across the Cenomanian-Turonian boundary (Ocean Drilling
601 Program Site 1138, Kerguelen Plateau). *Sedimentology* 64, 186–203.

602 Du Vivier, A.D., Selby, D., Sageman, B.B., Jarvis, I., Gröcke, D.R., Voigt, S., 2014. Marine
603 $^{187}\text{Os}/^{188}\text{Os}$ isotope stratigraphy reveals the interaction of volcanism and ocean
604 circulation during Oceanic Anoxic Event 2. *Earth Planet. Sci. Lett.* 389, 23–33.

605 Du Vivier, A. D. C., D. Selby, D. J. Condon, R. Takashima, and H. Nishi, 2015. Pacific
606 $^{187}\text{Os}/^{188}\text{Os}$ isotope chemistry and U–Pb geochronology: Synchronicity of global Os
607 isotope change across OAE 2, *Earth and Planetary Science Letters*, 428, 204–216.

608 Eicher, D.L., Worstell, P., 1970. Cenomanian and Turonian Foraminifera from the Great
609 Plains, United States. *Micropaleontology* 16, 269–324.

610 Ellwood, B.B., Crick, R.E., Hassani, A.E., Benoist, S.L., Young, R.H., 2000.
611 Magnetosusceptibility event and cyclostratigraphy method applied to marine rocks:
612 detrital input versus carbonate productivity. *Geology* 28, 1135–1138.

613 Ellwood, B.B., Tomkin, J.H., Ratcliffe, K.T., Wright, M., Kafafy, A.M., 2008. High-
614 resolution magnetic susceptibility and geochemistry for the Cenomanian/Turonian
615 boundary GSSP with correlation to time equivalent core. *Palaeogeogr. Palaeocl.* 261,
616 105–126.

617 Farrimond, P., Eglinton, G., Brassell, S., Jenkyns, H., 1990. The Cenomanian/Turonian
618 anoxic event in Europe: an organic geochemical study. *Marine and Petroleum Geology*
619 7, 75–89.

620 Fischer, A.G., 1986. Climatic rhythms recorded in strata. *Annu. Rev. Earth Planet. Sci.* 14,
621 351–376.

- 622 Gale, A.S., Christensen, W.K., 1996. Occurrence of the belemnite *Actinocamax plenus* in the
623 Cenomanian of SE France and its significance. *Bull. Geol. Soc. Denmark* 43, 68–77.
- 624 Gradstein, F.M., Ogg, J.G., Hilgen, F.J., 2012. On The Geologic Time Scale. *Newsl. Stratigr.*
625 45/2, 171–188.
- 626 Gröcke, D.R., 2002. The carbon isotope composition of ancient CO₂ based on higher-plant
627 organic matter. *Philos. Trans, series A, Math. Phys. Eng. Sci.* 360, 633–658.
- 628 Hasegawa, T., Seo, S., Moriya, K., Tominaga, Y., Nemoto, T., Naruse, T., 2010. High
629 resolution carbon isotope stratigraphy across the Cenomanian/Turonian boundary in the
630 Tappu area, Hokkaido, Japan: correlation with world reference sections. *Sci. Rep.*
631 Kanazawa University 54, 49–62.
- 632 Hasegawa, T., Crampton, J.S., Schiøler, P., Field, B., Fukushi, K., Kakizaki, Y., 2013. Carbon
633 isotope stratigraphy and depositional oxia through Cenomanian/Turonian boundary
634 sequences (Upper Cretaceous) in New Zealand. *Cretaceous Res.* 40, 61–80.
- 635 Hayes, J.M., Strauss, H., Kaufman, A.J., 1999. The abundance of ¹³C in marine organic
636 matter and isotopic fractionation in the global biogeochemical cycle of carbon during
637 the past 800 Ma. *Chem. Geol.* 161, 103–125.
- 638 Hikuroa, D., Crampton, P., Field, B., Schiøler, P., 2009. Upper Cretaceous oceanic red beds
639 in New Zealand. In: Hu, X., Wang, C., Scott, R.W., Wapreisch, M., Jansa, L. (Eds)
640 Cretaceous Oceanic Red Beds: Stratigraphy, Composition, and paleoceanographic and
641 paleoclimatic Significance, *SEPM Spec. Publ.* 91, 145–150.
- 642 Hu, X., Jansa, L., Wang, C., Sarti, M., Bak, K., Wapreisch, M., Michalik, J., Soták, J., 2005.
643 Upper Cretaceous oceanic red beds (CORBs) in the Tethys: occurrences, lithofacies,
644 age, and environments. *Cretaceous Res.* 26, 3–20.

645 Jenkyns, H.C., Matthews, A., Tsikos, H., Erel, Y., 2007. Nitrate reduction, sulfate reduction,
646 and sedimentary iron isotope evolution during the Cenomanian–Turonian oceanic
647 anoxic event. *Paleoceanography* 22, PA3208, doi: 10.1029/2006PA001355.

648 Jenkyns, H.C., 2010. Geochemistry of oceanic anoxic events. *Geochem. Geophys. Geosyst.*
649 11, Q03004, doi: 10.1029/2009GC002788.

650 Jenkyns, H.C., Dickson, A.J., Ruhl, M., Boorn, S.H.J.M., 2017. Basalt–seawater interaction,
651 the Plenus Cold Event, enhanced weathering and geochemical change: deconstructing
652 Oceanic Anoxic Event 2 (Cenomanian–Turonian, Late Cretaceous). *Sedimentology* 64,
653 16–43.

654 Jones, M. M., B. B. Sageman, R. L. Oakes, A. L. Parker, R. M. Leckie, T. J. Bralower, J.
655 Sepúlveda, and V. Fortiz, 2019. Astronomical pacing of relative sea level during
656 Oceanic Anoxic Event 2: Preliminary studies of the expanded SH#1 Core, Utah, USA,
657 *GSA Bulletin*, <https://doi.org/10.1130/B32057.1>.

658 Kuhnt, W., Luderer, F., Nederbragt, S., Thurow, J., Wagner, T., 2005. Orbital-scale record of
659 the late Cenomanian–Turonian oceanic anoxic event (OAE-2) in the Tarfaya Basin
660 (Morocco). *Int. J. Earth Sci.* 94, 147–159.

661 Kuroda, J., Ohkouchi, N., 2006. Implication of spatiotemporal distribution of black shales
662 deposited during the Cretaceous Oceanic Anoxic Event-2. *Paleontological Research* 10,
663 345–358.

664 Kuroda, J., Ogawa, N.O., Tanimizu, M., Coffin, M.F., Tokuyama, H., Kitazato, H., Ohkouchi,
665 N., 2007. Contemporaneous massive subaerial volcanism and late cretaceous Oceanic
666 Anoxic Event 2. *Earth Planet. Sci. Lett.* 256, 211–223.

667 Kuypers, M.M., Pancost, R.D., Nijenhuis, I.A., Sinninghe Damsté, J.S., 2002. Enhanced
668 productivity led to increased organic carbon burial in the euxinic North Atlantic basin
669 during the late Cenomanian oceanic anoxic event. *Paleoceanography* 17, 1051, doi:
670 10.1029/2000PA000569.

671 Laskar, J., Robutel, P., Joutel, F., Gastineau, M., Correia, A., Levrard, B., 2004. A long-term
672 numerical solution for the insolation quantities of the Earth. *Astron. Astrophys.* 428,
673 261–285.

674 Laskar, J., Fienga, A., Gastineau, M., Manche, H., 2011. La2010: a new orbital solution for
675 the long-term motion of the Earth. *Astronomy & Astrophysics* 532, A89, doi:
676 10.1051/0004-6361/201116836.

677 Li, X., Jenkyns, H.C., Wang, C., Hu, X., Chen, X., Wei, Y., Huang, Y., Cui, J., 2006. Upper
678 Cretaceous carbon-and oxygen-isotope stratigraphy of hemipelagic carbonate facies
679 from southern Tibet, China. *J. Geol. Soc. London* 163, 375–382.

680 Li, Y.-X., Montañez, I.P., Liu, Z., Ma, L., 2017. Astronomical constraints on global carbon-
681 cycle perturbation during Oceanic Anoxic Event 2 (OAE2). *Earth Planet. Sci. Lett.*
682 462, 35–46.

683 Lyle, M., 1983. The brown–green color transition in marine sediments: A marker of the
684 Fe(III)–Fe(II) redox boundary1. *Limnol. Oceanogr.* 28, 1026–1033.

685 Ma, C., S. R. Meyers, B. B. Sageman, B. S. Singer, and B. R. Jicha, 2014. Testing the
686 astronomical time scale for oceanic anoxic event 2, and its extension into Cenomanian
687 strata of the Western Interior Basin (USA), *Bulletin*, 126 (7–8), 974–989.

688 Meyers, S.R., Sageman, B.B., Hinnov, L.A., 2001. Integrated quantitative stratigraphy of the
689 Cenomanian-Turonian Bridge Creek Limestone Member using evolutive harmonic
690 analysis and stratigraphic modeling. *J. Sediment. Res.* 71, 628–644.

691 Meyers, S. R., S. E. Siewert, B. S. Singer, B. B. Sageman, D. J. Condon, J. D. Obradovich, B.
692 R. Jicha, and D. A. Sawyer, 2012. Intercalibration of radioisotopic and astrochronologic
693 time scales for the Cenomanian-Turonian boundary interval, Western Interior Basin,
694 USA, *Geology*, 40(1), 7–10.

695 Monteiro, F., Pancost, R., Ridgwell, A., Donnadieu, Y., 2012. Nutrients as the dominant
696 control on the spread of anoxia and euxinia across the Cenomanian–Turonian oceanic

697 anoxic event (OAE2): Model–data comparison. *Paleoceanography* 27, PA4209, doi:
698 10.1029/2012PA002351.

699 Navarro-Ramirez, J.P., Bodin, S., Immenhauser, A., 2016. Ongoing Cenomanian — Turonian
700 heterozoan carbonate production in the neritic settings of Peru. *Sediment. Geol.* 331,
701 78–93.

702 Navarro-Ramirez, J., Bodin, S., Consorti, L., Immenhauser, A., 2017. Response of western
703 South American epeiric-neritic ecosystem to middle Cretaceous Oceanic Anoxic
704 Events. *Cretaceous Res.* 75, 61–80.

705 Obradovich, J., 1993. A Cretaceous time scale, in *Evolution of the Western interior Basin:*
706 *Geological Society of Canada Special Paper 39*, edited by W. G. E. Caldwell and E. G.
707 Kauffmann, pp. 379–396.

708 Pogge von Strandmann, P.A.E., Jenkyns, H.C., Woodfine, R.G., 2013. Lithium isotope
709 evidence for enhanced weathering during Oceanic Anoxic Event 2. *Nat. Geosci.* 6, 668.

710 Prokoph, A., Babalola, L.O., El Bilali, H., Olagoke, S., Rachold, V., 2013. Cenomanian–
711 Turonian carbon isotope stratigraphy of the Western Canadian Sedimentary Basin.
712 *Cretaceous Res.* 44, 39–53.

713 Sageman, B.B., Meyers, S.R., Arthur, M.A., 2006. Orbital time scale and new C-isotope
714 record for Cenomanian-Turonian boundary stratotype. *Geology* 34, 125–128.

715 Scaife, J., Ruhl, M., Dickson, A., Mather, T., Jenkyns, H., Percival, L., Hesselbo, S.,
716 Cartwright, J., Eldrett, J., Bergman, S., 2017. Sedimentary Mercury Enrichments as a
717 Marker for Submarine Large Igneous Province Volcanism? Evidence From the Mid-
718 Cenomanian Event and Oceanic Anoxic Event 2 (Late Cretaceous). *Geochem. Geophys.*
719 *Geosyst.* 18, 4253–4275.

720 Schiøler, P., and Crampton J. S., 2014. Dinoflagellate biostratigraphy of the Arowhanan Stage
721 (upper Cenomanian–lower Turonian) in the East Coast Basin, New Zealand, *Cretaceous*
722 *Research*, 48(Supplement C), 205–224.

723 Schlanger, S., Jenkyns, H., 1976. Cretaceous oceanic anoxic events: causes and
724 consequences. *Geol. Mijnb.* 55, 179–194.

725 Schlanger, S., Arthur, M., Jenkyns, H., Scholle, P., 1987. The Cenomanian-Turonian Oceanic
726 Anoxic Event, I. Stratigraphy and distribution of organic carbon-rich beds and the
727 marine $\delta^{13}\text{C}$ excursion. In: Brooks, J, Fleet, A.J. (Eds) *Marine Petroleum Source Rocks*,
728 *Geol. Soc., London, Special Publication 26*, 371–399.

729 Scholle, P.A., Arthur, M.A., 1980. Carbon isotope fluctuations in Cretaceous pelagic
730 limestones: potential stratigraphic and petroleum exploration tool. *AAPG Bull.* 64, 67–
731 87.

732 Sinninghe Damsté, J.S., van Bentum, E.C., Reichart, G.-J., Pross, J., Schouten, S., 2010. A
733 CO₂ decrease-driven cooling and increased latitudinal temperature gradient during the
734 mid-Cretaceous Oceanic Anoxic Event 2. *Earth Planet. Sci. Lett.* 293, 97–103.

735 Sutherland, R., 1999. Basement geology and tectonic development of the greater New
736 Zealand region: an interpretation from regional magnetic data. *Tectonophysics* 308,
737 341–362.

738 Sweere, T.C., Dickson, A.J., Jenkyns, H.C., Porcelli, D., Elrick, M., van den Boorn, S.H.,
739 Henderson, G.M., 2018. Isotopic evidence for changes in the zinc cycle during Oceanic
740 Anoxic Event 2 (Late Cretaceous). *Geology* 46, 463–466.

741 Takashima, R., H. Nishi, T. Yamanaka, T. Tomosugi, A. G. Fernando, K. Tanabe, K. Moriya,
742 F. Kawabe, and K. Hayashi, 2011. Prevailing oxic environments in the Pacific Ocean
743 during the mid-Cretaceous Oceanic Anoxic Event 2, *Nature Communications*, 2, 234.

744 Tsikos, H., Jenkyns, H., Walsworth-Bell, B., Petrizzo, M., Forster, A., Kolonic, S., Erba, E.,
745 Silva, I.P., Baas, M., Wagner, T., 2004. Carbon-isotope stratigraphy recorded by the
746 Cenomanian–Turonian Oceanic Anoxic Event: correlation and implications based on
747 three key localities. *J. Geol. Soc. London* 161, 711–719.

748 Turgeon, S.C., Creaser, R.A., 2008. Cretaceous oceanic anoxic event 2 triggered by a massive
749 magmatic episode. *Nature* 454, 323–326.

750 Voigt, S., Aurag, A., Leis, F., Kaplan, U., 2007. Late Cenomanian to Middle Turonian high-
751 resolution carbon isotope stratigraphy: New data from the Münsterland Cretaceous
752 Basin, Germany. *Earth and Planetary Science Letters* 253, 196–210.

753 Voigt, S., Erbacher, J., Mutterlose, J., Weiss, W., Westerhold, T., Wiese, F., Wilmsen, M.,
754 Wonik, T., 2008. The Cenomanian–Turonian of the Wunstorf section–(North
755 Germany): global stratigraphic reference section and new orbital time scale for Oceanic
756 Anoxic Event 2. *Newsletters on Stratigraphy* 43, 65–89.

757 Wang, C., Hu, X., Huang, Y., Scott, R.W., Wagreich, M., 2009. Overview of Cretaceous
758 Oceanic Red Beds (CORBs): a window on global oceanic and climate change. In: Hu,
759 X., Wang, C., Scott, R.W., Wagreich, M., Jansa, L. (Eds) *Cretaceous Oceanic Red
760 Beds: Stratigraphy, Composition, and paleoceanographic and paleoclimatic
761 Significance*, SEPM Spec. Publ. 91, 13–33.

762 Zhou, X., Jenkyns, H.C., Owens, J.D., Junium, C.K., Zheng, X.Y., Sageman, B.B., Hardisty,
763 D.S., Lyons, T.W., Ridgwell, A., Lu, Z., 2015. Upper ocean oxygenation dynamics
764 from I/Ca ratios during the Cenomanian–Turonian OAE 2. *Paleoceanography* 30, 510–
765 526.

766

FIGURE CAPTIONS:

Fig. 1: (a) Palaeogeographic reconstruction of the Cretaceous denoting section locations: Colorado, Western Platform, Tarfaya, Eastbourne, Gongzha, Tappu, Mangaotane B and Sawpit Gully (modified from Zhou et al., 2015). (b) Carbonate carbon-isotope stratigraphy from Eastbourne, UK (Tsikos et al., 2004). (c) Map of central New Zealand showing the sampling sites Mangaotane B and Sawpit Gully. Grey shading indicates Albian–Maastrichtian (113–66 Ma) sedimentary marine successions (modified from Hasegawa et al., 2013).

Fig. 2: Photograph, taken in a westerly direction, of the main red-bed in the Mangaotane B section, which has a stratigraphic thickness of ~29–36 m.

Fig. 3: Stratigraphy, magnetic susceptibility (MS), weight-per-cent total organic carbon (wt % TOC) and $\delta^{13}\text{C}_{\text{TOC}}$ data relative to Vienna Pee Dee Belemnite (V-PDB) from Mangaotane B from samples collected in 2015. Error bars correspond to 1 SD. Coloured bands describe the carbon-isotope stages.

Fig. 4: Map of Sawpit Gully, Marlborough, showing the locations of the sampling transects. Inset map shows part of NZ Topo50 map sheet BS28, Kekerengu, and the 1 km NZ map grid, to facilitate location of the main figure.

Fig. 5: Map of Mangaotane B, Raukumara Peninsula, showing the locations of the sampling transects. Inset map shows part of the NZ Topo50 map sheet BE42, Haupoto, and the 1 km NZ map grid, to facilitate location of the main figure.

Fig. 6: Stratigraphy, magnetic susceptibility (MS), weight-per-cent total organic carbon (wt % TOC) and $\delta^{13}\text{C}_{\text{TOC}}$ data relative to Vienna Pee Dee Belemnite (V-PDB) from Sawpit Gully (samples collected in 2015 and 2016) correlated with the $\delta^{13}\text{C}_{\text{carb}}$ stratigraphy from Tibet (Li et al., 2017). Error bars correspond to 1 SD. Coloured bands describe the carbon-isotope stages, which include a relatively sharp initial increase (yellow), a trough (red), a plateau (green) and a gradual decrease to pre-excursion values with an average of ca. -25 ‰ (blue). The main OAE 2 stages shown as coloured bands result from correlation to the Eastbourne section, as discussed in Section 5.4. The Tibetan succession provides ages at the onset and end of the CIE used to create a linear age model for the Sawpit Gully record. See Fig. 3 for the remainder of the legend.

Fig. 7: Cross-plot of HI and T_{max} of selected samples from Sawpit Gully and Mangaotane B, whose contained organic matter is most likely of terrestrial origin.

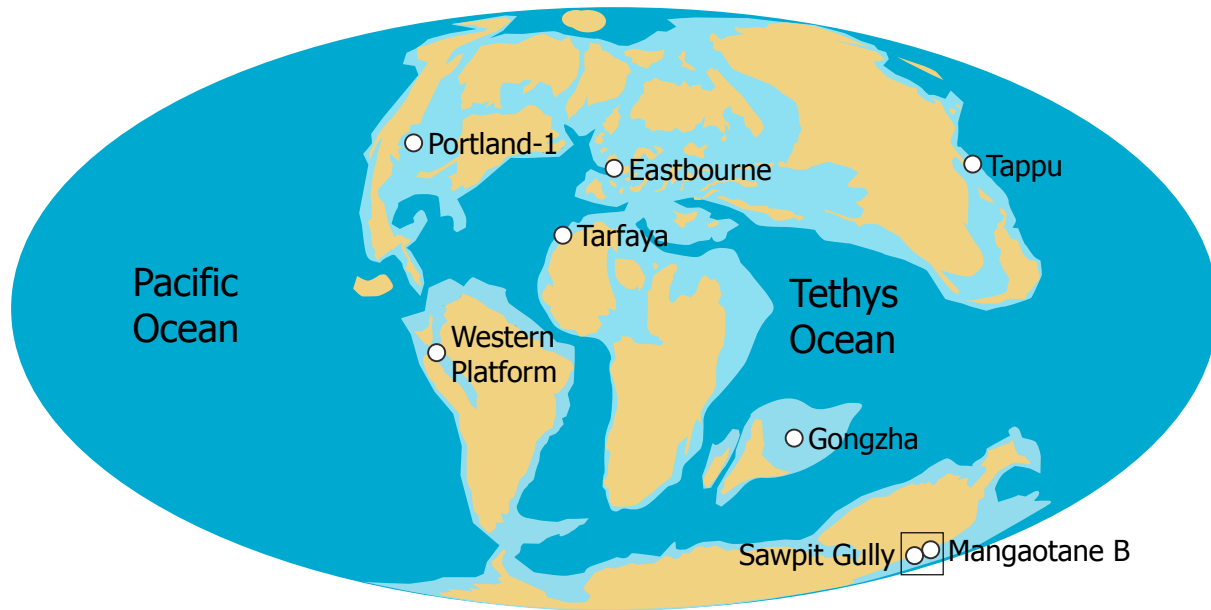
Fig. 8: Comparison between the carbon-isotope stratigraphy of A) carbonate carbon from Eastbourne, UK (Tsikos et al., 2004); B) marine organic carbon from S75, Tarfaya Basin, SW Morocco (Kuhnt et al., 2005); C) marine organic carbon from Portland-1, Colorado, USA (Sageman et al., 2006); D) terrestrial organic carbon from Sawpit Gully, New Zealand (this study); E) marine and terrestrial organic carbon from Mangaotane B, New Zealand (this study); black data points derive from samples with TOC > 0.1 wt % representing global

signatures; grey data points derive from samples with TOC \leq 0.1 wt %); F) terrestrial organic carbon from Tappu, Hokkaido, Japan (Hasegawa et al., 2010; Nemoto and Hasegawa, 2011); G) marine organic carbon from Quebrada Chinchin and Piedra Parada, Western Platform, northern Peru (Navarro-Ramirez et al., 2016, 2017) and H) carbonate carbon from Gongzha, southern Tibet (Li et al., 2017). Squares in the Sawpit Gully and Mangaotane B sections show the data from Hasegawa et al. (2013). Coloured bands describe the carbon-isotope stages.

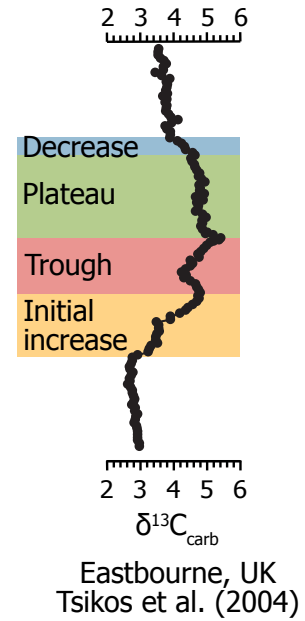
Fig. 9: (a) Spectral analysis of the main part of the $\delta^{13}\text{C}_{\text{TOC}}$ excursion (CIE) across the OAE 2 interval from Sawpit Gully reveals three statistically significant cycles. Only the 3.9 m cycle is interpreted to be of relevance (see Supplementary Material for details) (b) Spectral analysis of the age-corrected MS data from Sawpit Gully identifies a 38 ky obliquity cycle and a 21 ky precession cycle.

Fig. 10: $\delta^{13}\text{C}_{\text{TOC}}$ age model for Sawpit Gully giving a duration of the CIE as a minimum of 930 ± 25 ky and the position of the Cenomanian–Turonian boundary (dated at 93.9 Ma (Obradovich et al., 1993; Gradstein et al., 2012; Meyers et al., 2012)) in the second half of the plateau. A comparison of the filtered temporal $\delta^{13}\text{C}_{\text{TOC}}$ record and the filtered eccentricity (Laskar et al., 2004) shows that the $\delta^{13}\text{C}_{\text{TOC}}$ is in phase with the orbital record and has similar relative amplitude variations. The filtered and unfiltered eccentricity (Laskar et al., 2004) shows weak cycles from around 94.1 Ma to 93.9 Ma.

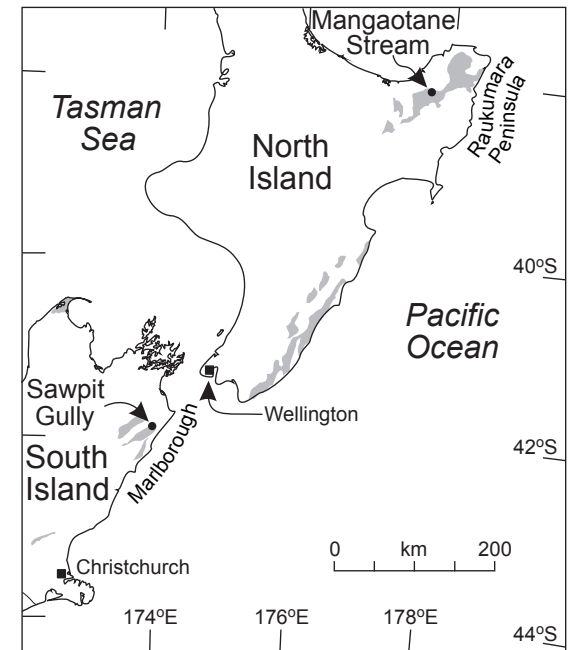
(a)



(b)

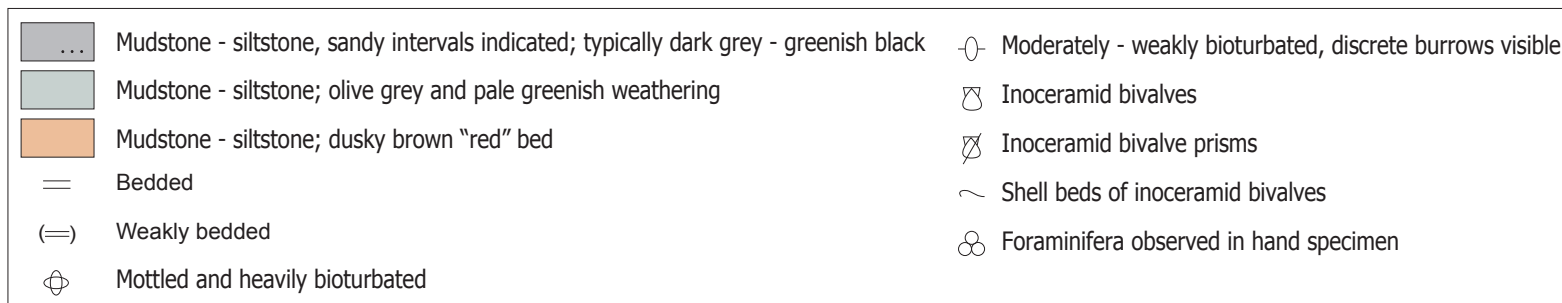
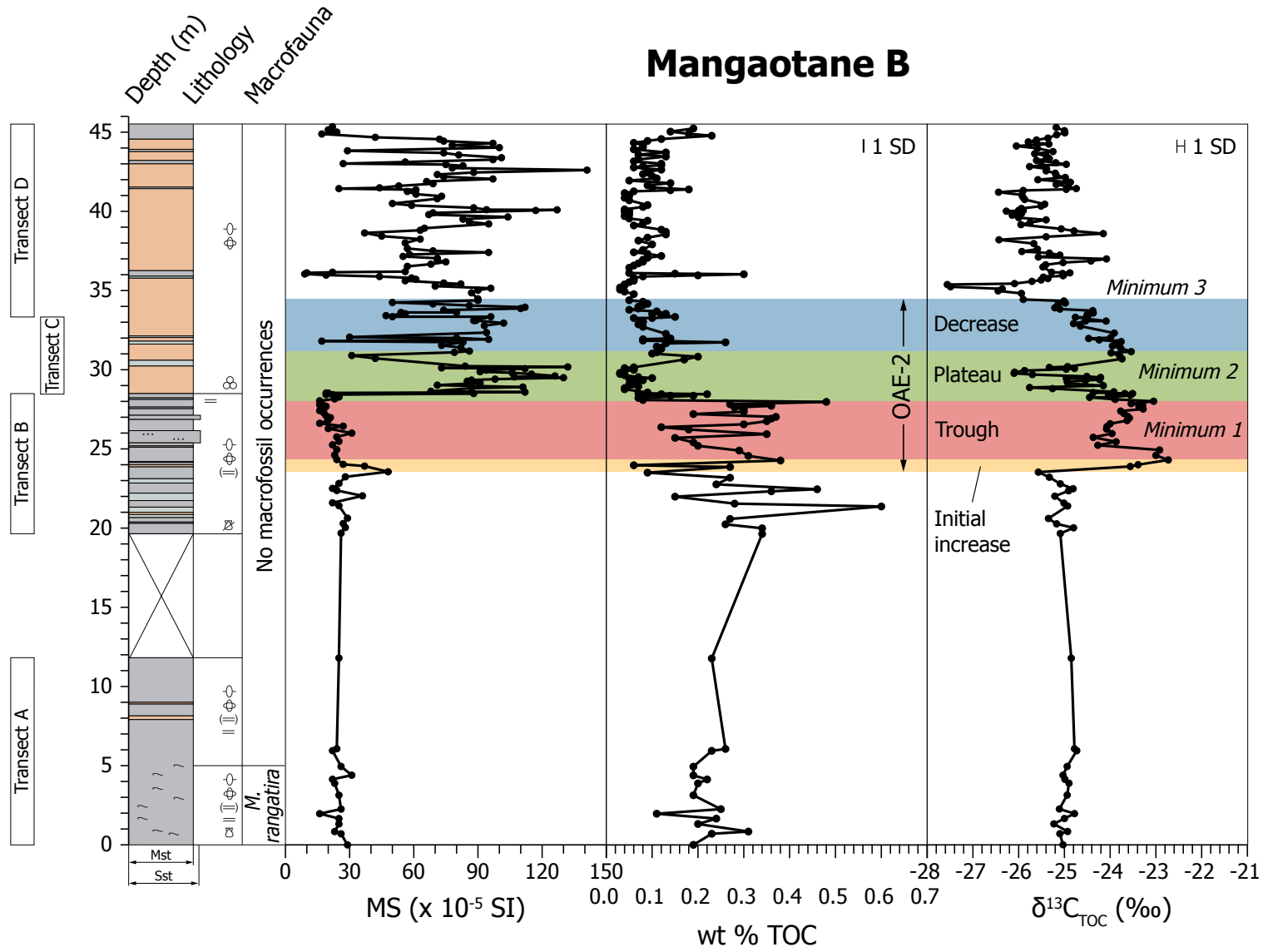


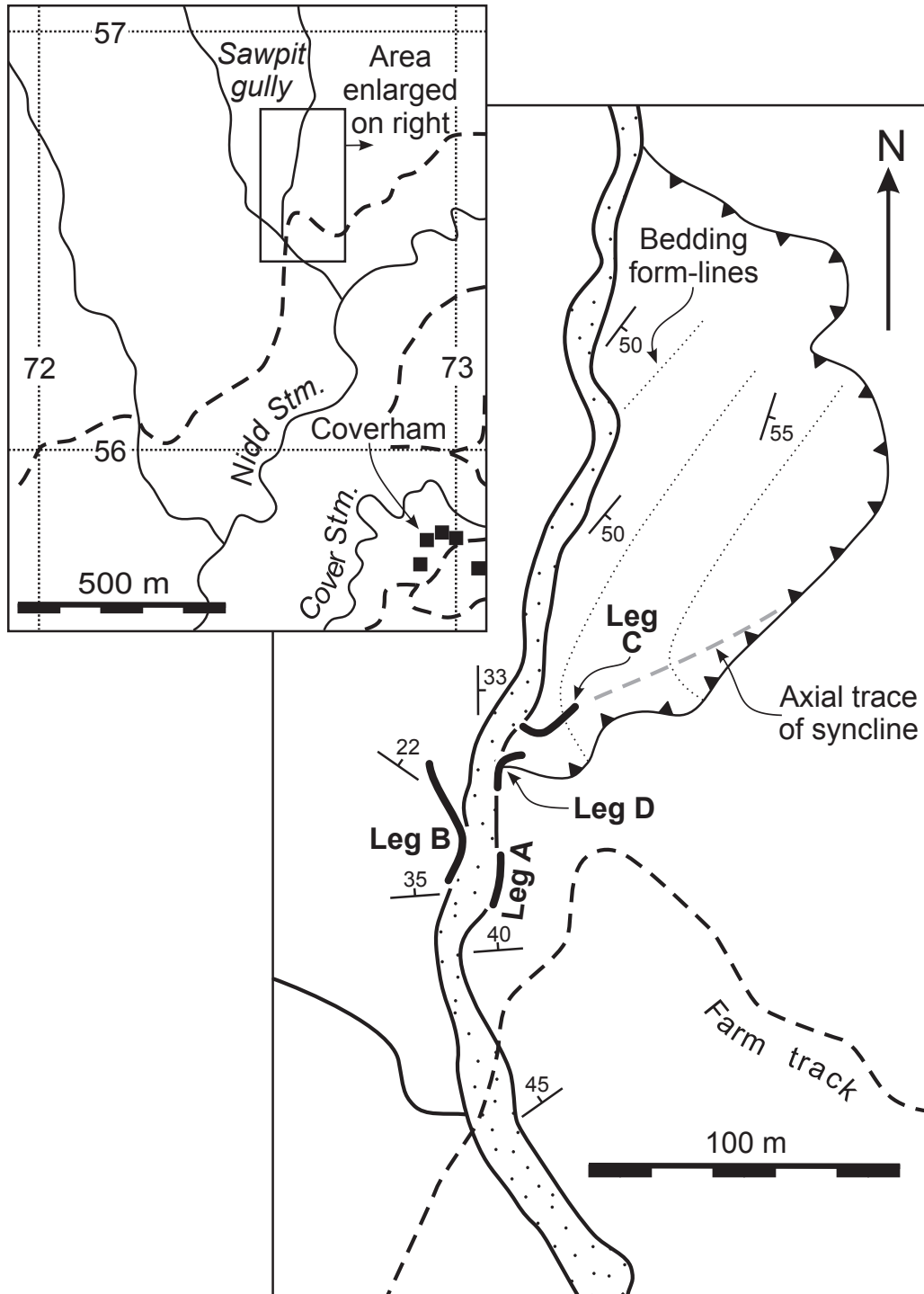
(c)

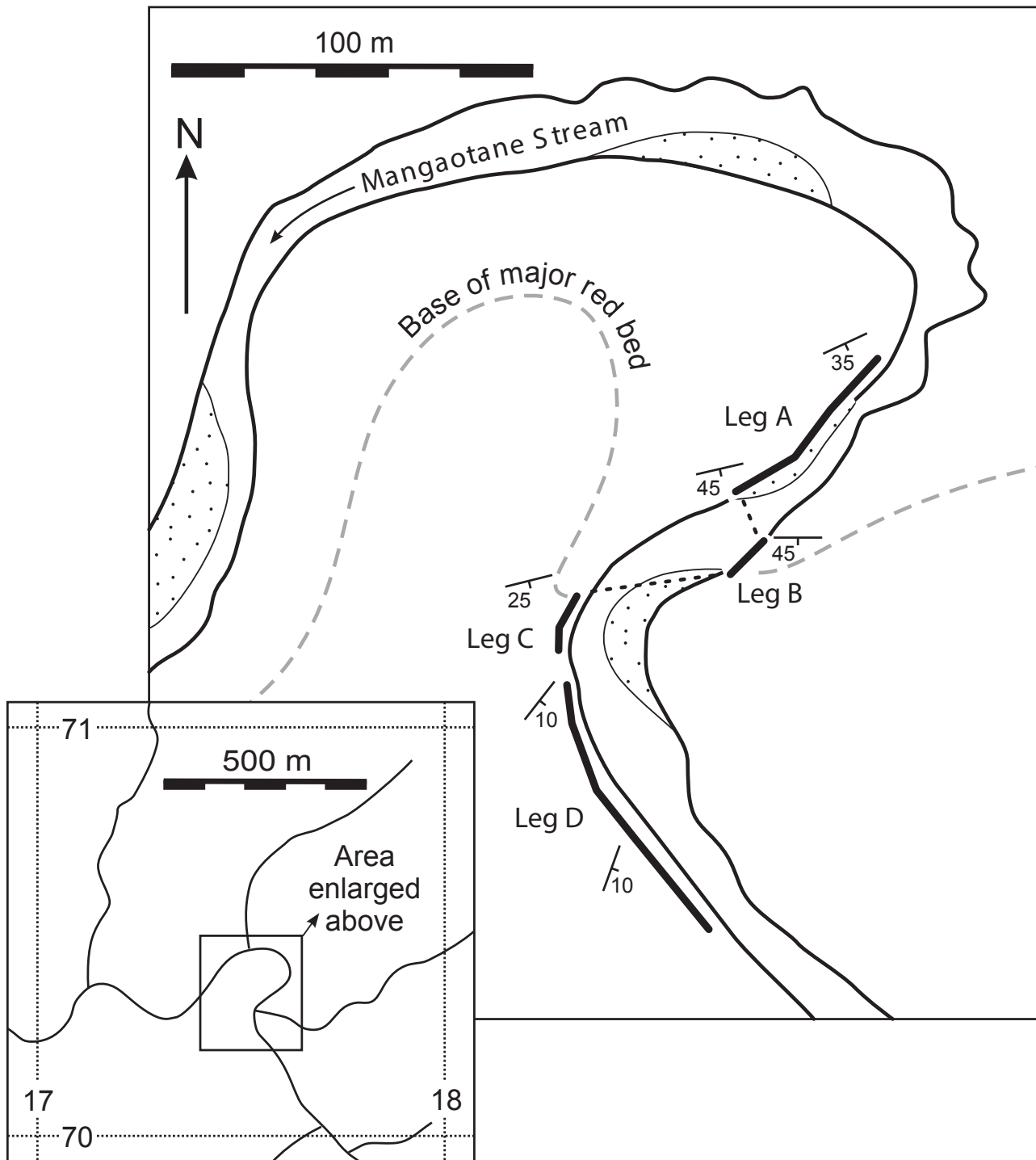




Mangaotane B







Sawpit Gully

